INVESTIGATION ON SENSOR SELECTION APPLIED ON A VEHICLE-AS-A-SENSOR CONCEPT IN HIGH-SPEED FLIGHT

Ana C. Meinicke[1] and Carlos E. S. Cesnik[1]

[1]University of Michigan
Ann Arbor, Michigan, USA
meinicke@umich.edu
cesnik@umich.edu

Keywords: Neural network, sensor selection, strain, temperature

Abstract: The ability to estimate aerodynamic loads and flight parameters in flight using only internal sensors is desirable for guidance, navigation, and control. This is particularly true for harsh aerothermal environments experienced in supersonic and hypersonic flight, but it is also applicable to any other flight regime. The vehicle-as-a-sensor concept is a novel nonintrusive sensing strategy for airframes in flight. It leverages the internal measurement of the deformed state of the vehicle, its temperatures, and its accelerations to infer its aerodynamic state. An inverse model consisting of a strain-to-load, or strain/temperature-to-load, neural network trained with static elastic solutions of a detailed finite element model of a slender hypersonic vehicle is considered here. The deformed state of the vehicle is assumed to be measured with high-density strain and temperature measurements on its internal surface, enabled by the application of continuous fiber optic sensors. Constraints pertaining to the use of fiber optic sensors are considered, where limitations such as applying the optical cables only on the internal surface of the vehicle, and the necessity of choosing adequate strain component directions to recover the aerodynamic state with sufficient accuracy are accounted for. Inverse models considering selected sensors based on the physics involved in the problem are shown to successfully recover pressure distribution on the outer surface of the vehicle.

1 INTRODUCTION

High-speed flight conditions are challenging environments when it comes to designing aircraft and their flight control systems. More specifically, temperatures on the outer surface of a vehicle in hypersonic conditions can reach around 1400°C due to heating [1]. This greatly affects design choices such as materials and sensor selection.

To tackle this problem, a novel vehicle-as-a-sensor concept [2] is explored. It uses the vehicle's own deformation to obtain the aerodynamic loads it is subjected to by solving an inverse problem. Pham et al. [2] showed that this can be achieved by using machine learning algorithms and successfully recovered pressure loads on a vehicle in hypersonic conditions given strain measurements. However, no thermal effects were considered in that study.

In these high-speed flight conditions, thermal effects actually fundamentally change the nature of the problem, and the vehicle's dynamics. It becomes necessary to consider the aerodynamics, aerodynamic heating, heat transfer, and the elastic airframe, as well as the interactions between each of these [3] since the problem is highly coupled [4].

Inverse elasticity problems of similar nature have been addressed previously through the use of finite element models (FEM) with regularization in an iterative manner [5]. Still using finite element models, inverse problems were addressed based on an inverse interpolation approach to define loads through least-squares minimization of calculated and measured strains [6]. With a non-iterative manner, it has also been addressed using deformations and tractions considering the boundary element method [7].

Other recent attempts at addressing the solution of the inverse problem also leveraged on the linearity assumption of the elastic structural model, while accounting for its ill-posedness. Pham et al. [8] approached it as a least-squares problem and used finite element method solutions of the elasticity partial differential equation as a constraint. Panigrahi et al. [9] applied a data-driven technique for force reconstruction on a beam-like structure based on the pseudo-inverse of the flexibility influence coefficients matrix.

For the vehicle-as-a-sensor to work, the solution of the inverse problem needs to be quick (in real time), account for nonlinearities that arise from considering thermal effects, and possibly account for unsteady effects.

Machine learning algorithms can satisfy these necessities if trained on relevant physics informed data. Raissi et al. [10] showed that neural networks (NNs) can be used to provide solutions for forward and inverse problems modeled by partial differential equations including nonlinearities. On a more similar application to inferring loads for flight control purposes, Singh and Willcox [11] applied machine learning, Bayesian statistics, and decision theory to perform trajectory adjustments on a vehicle given in-flight measurements.

Neural networks have been used before to identify loads on aircraft-like structures given strain measurements by Cao et al. [12], as well as by Klotz et al. [13] to obtain wing twist angle given strain measured with a fiber optic sensing system on a modern business jet.

Thus, neural networks are proposed and applied here as a solution to the inverse problem that defines the vehicle-as-a-sensor concept. They provide a mapping between the measured internal strain and temperature of the structure to the applied aerodynamic loads.

The training data necessary for the neural network model are based on a detailed FEM of the vehicle, where several responses to applied loads are generated so that an accurate mapping can be obtained. It is generated through a framework based on the University of Michigan's High-Speed Vehicle (UM/HSV) simulation framework [14]. Pressure loads are generated using Newtonian impact theory with shock-expansion pressure relations [15] and they are applied to the structural FEM model of the vehicle to generate the corresponding static deformation solution.

The definition of sensor placement is crucial to obtain an accurate and effective solution for the inverse model and the vehicle-as-a-sensor. While Pham et al. [8] and Panigrahi et al. [9] have provided insights into obtaining optimized placements considering their strain-to-load mappings, no considerations have been made regarding the thermal effects and temperature sensors.

The process for obtaining the inverse model through a neural network and the generation of training data is described in Section 2, where the approach for including thermal effects is also detailed. Section 3 explores the sensor selection methodologies, and Section 4 defines the vehicle used to exercise the proposed methods and presents the results.

2 NEURAL NETWORK-BASED INVERSE MODEL

To address the need for an inverse model that enables the vehicle-as-a-sensor concept, the use of neural networks is introduced. They are known to be of quick response once trained, and being capable of modeling non-linearities, which align with the requirements of the problem at hand. Potential difficulties of applying neural networks can arise from the loss of interpretability of the model, and the need for large and accurate amounts of training data.

To simplify the problem for the current evaluations, only steady state conditions are considered, and no distributed inertial effects are included. But the framework is general enough that it can be enhanced to include those in a similar way.

The framework for generating the training data is described in Subsection 2.1, the approach for including thermal effects is detailed in Subsection 2.2, and the neural network-based inverse model is defined in Subsection 2.3.

2.1 Generation of Training Data

The main framework used to generate the training data is represented in Figure 1. The process starts with sampling the parameter space experienced in flight, by defining Mach number, altitude, angle of attack, and angle of sideslip. Then, parts of UM/HSV are used to obtain a trimmed condition of the vehicle if desired, and obtain the aerodynamic loads the vehicle is subjected to by applying Newtonian impact theory with shock-expansion pressure relations. Additional adjustments could be made to the loads to account for separation, if high-fidelity numerical solutions or experimental observed loads are available for the vehicle of interest. The impact of using aerodynamic loads of reduced accuracy has been assessed and addressed in previous work [16].
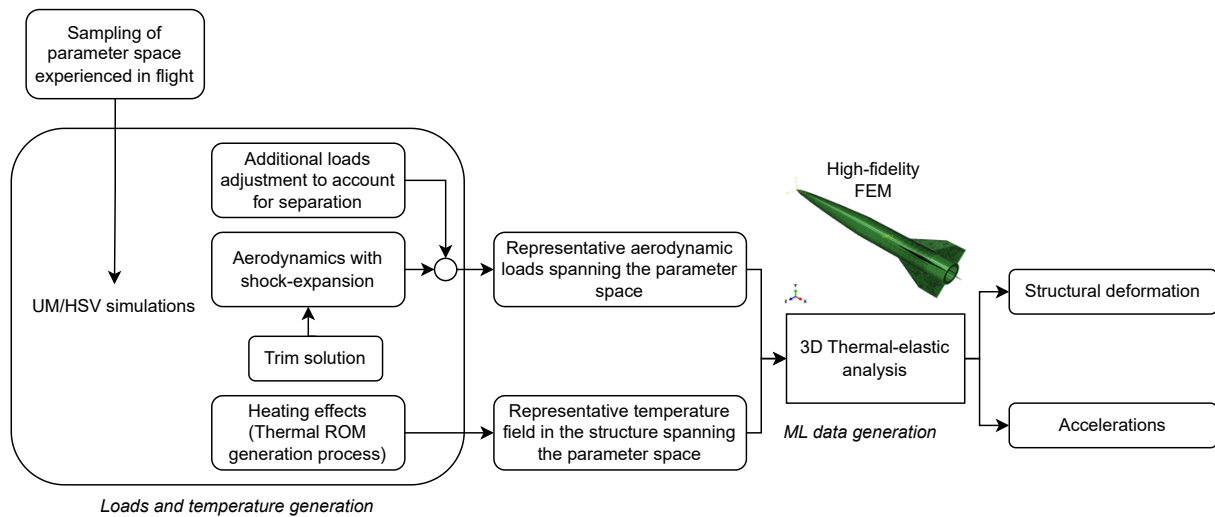

Figure 1: Framework for generating training data.

Heating effects are included through a thermal reduced order model (ROM) generation process proposed by Falkiewicz and Cesnik [3]. This ROM is used to generate temperature fields that are considered representative of what could be encountered in flight. This process is further described in Subsection 2.2.

The temperature fields and the aerodynamic loads are applied to the high-fidelity FEM for a

thermal-elastic solution. Outputs of interest for this solution include strain and equivalent rigid body acceleration, since a free-flight boundary condition is imposed.

The aerodynamic pressure on the outer surface affects the heating loads, and this is modeled through the thermal ROM generation process used in this framework. However, the heating loads do not considerable affect the aerodynamic pressure. This enables the application of the current framework, where the temperature fields and the aerodynamic loads are applied to the FEM independently.

2.2 Inclusion of Thermal Effects

It is necessary to account for the high temperatures experienced during high speed flight conditions since they affect the mechanical and thermal properties of the materials, and consequently, the deformation and strain experienced by the vehicle in flight. To properly account for that, it is important to model the geometric stiffening that results from the thermal expansion in the structure due to the temperature distribution, the change in material properties, and the applied thermal loads.

To generate the representative temperature fields in the structure, the thermal model generated by Weston and Cesnik [17] is used. It builds on the procedure proposed by Falkiewicz and Cesnik [3], where thermal snapshots are obtained from a series of independent aero-thermo-elastic simulations of flight trajectories of interest. This is followed by applying proper orthogonal decomposition (POD) to obtain a modal subspace of lower dimensionality.

Combinations of the thermal modes with modal coordinates ranging between the bounds corresponding to the snapshots are used to generate the temperature fields. The modal coordinates are obtained through Latin hypercube sampling (LHS). Temperature fields with unrealistic values are discarded, that is, only fields where $0 < T < 1000$ K are kept. Once the temperature fields are generated, thermal-elastic solutions are obtained using Abaqus [18], where the necessary considerations to account for the thermal effects for a free-flight boundary condition are represented in Figure 2.
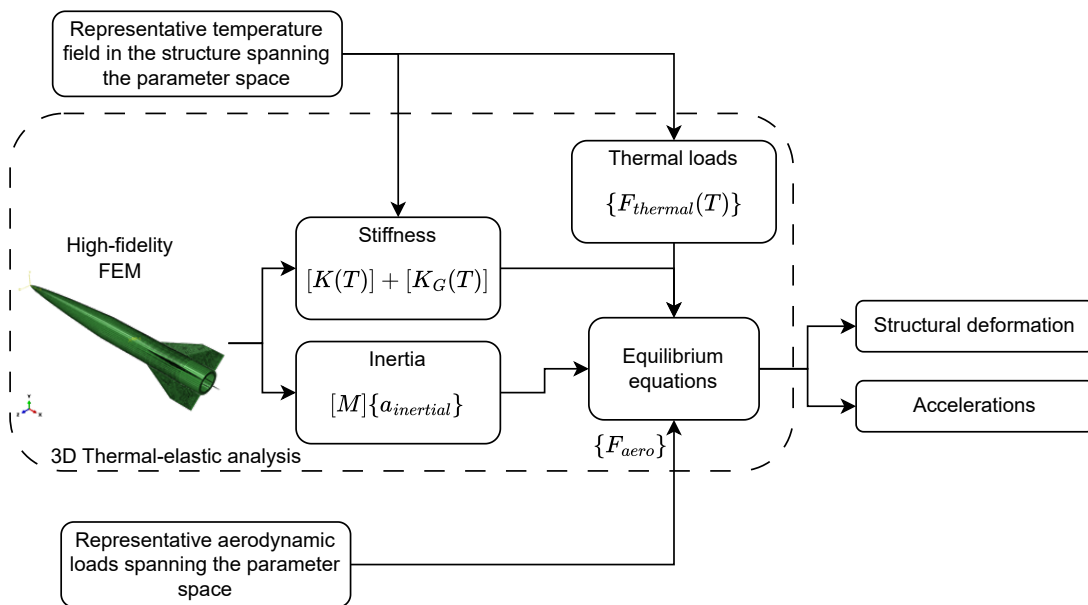

Figure 2: High-fidelity FEM thermal-elastic solution.

The temperature field enters as thermal loads to the model and as changes to the material properties in the temperature dependent stiffness matrices. The aerodynamic loads enter as external nodal forces. Once the loads are defined, the equilibrium equations are solved and the outputs of interest are obtained.

In order to be comprehensive of the flight conditions of interest, a large number of temperature fields is expected to be needed, and more combinations of temperature fields and aerodynamic loads than what would be observed in flight should be considered.

2.3 Neural Network: Strain- and Temperature-to-Pressure Distributions

Figure 2 is a representation of the forward model, where loads are used as input to a FEM solution, and strains can be obtained as outputs. This input-output pair constitutes the training data necessary for obtaining the inverse model, modeled here through a neural network.

A feedforward fully connected neural network for regression is obtained using Bayesian optimization with a 5-fold cross validation, where the number of layers can vary from 1 to 5, the size of each layer can vary from 1 to 400, the activation function can be one from Rectified Linear Unit (ReLU), hyperbolic tangent, sigmoid or none, and standardization and regularization can be applied or not.

The training data for this inverse model is defined as strain and temperature values from selected nodes on the inner surface of the vehicle FEM, and pressure distribution on the outer surface of the vehicle. It maps strain and temperature measurements to the aerodynamic load the vehicle is subjected to at that instant.

To decrease the dimensionality of the problem, a POD of the pressure values is obtained. This allows for the recovery of modal coordinates instead of discretized pressure values on the outer surface of the vehicle. Similarly, the recovery of integrated or distributed forces is also possible.

3 SENSOR SELECTION

For an accurate and practical solution of the inverse problem, it is crucial to select relevant and sufficient number of sensor points as inputs. Thus, sensor selection is addressed here.

A common sensor selection methodology consists of applying an observability analysis. While promising for the current application, it requires a state space representation of the system, which is currently not implemented.

One disadvantage of using machine learning algorithms such as neural networks is that they are known to loose interpretability, making it difficult to use in sensor placement, or sensor selection. While SHAP (SHapley Additive exPlanations) [19], a framework designed for interpreting model predictions, addresses this issue, its implementation quickly becomes unfeasible as hundreds of inputs are considered in the model.

A straightforward method of obtaining the influence each sensor has on a determined output load was applied by Panigrahi et al. [9], where a heat map of the pseudo-inverse of the Flexibility Influence Coefficients matrix was presented. This matrix can be determined by training data consisting of applied loads and resulting strain. However, the method assumes linearity between the input and output, meaning it cannot be applied in the presence of thermal effects.

To overcome that, the problem is divided into two parts. First, the nodes are ranked according to the heat map, considering strain data without any thermal effects. In parallel, the nodes are

ranked through an equivalent heat map generated considering the previously mentioned thermal modes.

This process, although simplistic, is applicable to this problem and is further detailed in Subsection 3.1 and Subsection 3.2, along with the metric of error given the retained number of nodes. For both parts, only sensor points on the inner surface of the vehicle comprise the initial set that is then ranked.

3.1 Strain

As applied by Panigrahi et al. [9], the heat map of the pseudo-inverse of the Flexibility Influence Coefficients matrix $[C]$ is used here. First, $[C]$ is obtained based on the training data with

$$[C_{i\times a}] = \{\varepsilon_{i\times n}\}\{f_{a\times n}\}^T(f_{a\times n}f_{a\times n}^T)^{-1}, \tag{1}$$

where ε represents the strain, and f represents the applied load. The subindices i correspond to the number of inputs, a to the number of outputs, and n to the number of training cases.

The pseudo-inverse of $[C]$ can be used to obtain recovered loads with

$$\{f_{r_{a\times n}}\} = (C_{i\times a}^T C_{i\times a})^{-1}C_{i\times a}^T\{\varepsilon_{i\times n}\} = [C_{a\times i}^+]\{\varepsilon_{i\times n}\}. \tag{2}$$

Now, $[C^+]$ provides a heat map with a metric of influence of each strain sensor and component to the applied/recovered load.

For the problem at hand, the applied loads can be defined as pressure distribution on the outer surface of the vehicle, or force distribution decomposed in each direction. Since this method assumes linearity, force is used instead of pressure. And the force distribution is modeled through POD modes, similarly to what is applied to the pressure distribution in Subsection 2.3.

The sensors can then be ranked according to the influence value in matrix $[C^+]$. After ranked by importance, the sensors can be selected, and Equations 1 and 2 can be applied once again. A metric of error can then be obtained when comparing the recovered forces to the original forces.

3.2 Temperature

The same heat map concept is applied to the temperature sensor selection. However, the $[C]$ matrix in this case actually corresponds to the thermal bases, that is, the thermal modes of the model referred to in Subsection 2.2.

Sensor points are then ranked and can be selected by importance. The recovered thermal modes can be obtained from

$$[\phi_{r_{i\times a}}] = \{T_{i\times n}\}\{c_{a\times n}\}^T(c_{a\times n}c_{a\times n}^T)^{-1}, \tag{3}$$

where T are the temperature fields with selected sensors and c correspond to the modal coordinates used to generate the respective fields. The subindices i correspond to the number of sensor points, a to the number of thermal modes, and n to the number of training cases.

The recovered modal coordinates are obtained from

$$\{c_{r_{a\times n}}\} = ([\phi_{r_{i\times a}}]^T[\phi_{r_{i\times a}}])^{-1}[\phi_{r_{i\times a}}]^T\{T_{i\times n}\}. \tag{4}$$

The error metric is obtained by comparing the recovered modal coordinates with the initial modal coordinates.

4 RESULTS

The Initial Concept 3.X (IC3X), a representative slender high-speed vehicle, is used as a test case. The results presented next are based on a FEM of the IC3X from Klock and Cesnik [20]. The model contains a total of 80,940 nodes and 66,045 elements, consisting of tetrahedral, hexahedral and wedge shapes.

Training data is generated for combinations of $M = [5, 6, 7]$, $h = [20, 25, 30, 35, 40]$ km, and $\alpha = [0°, 10°, 20°, 30°]$, resulting in a total of 60 flight conditions. Notably, the trajectories used by Weston and Cesnik [17] for the generation of the thermal model also span these conditions.

In the next subsections, results regarding the inclusion of thermal effects are explored, followed by results on the sensor selection methodology applied on the strain sensors and then on temperature sensors, and finally, results on the recovery of pressure distribution using the inverse model, as well as comparisons on the use of different sensor sets are explored.

4.1 Inclusion of Thermal Effects

The effect of including thermal loads on the training data generation process can be evaluated when strain values obtained with and without thermal effects are compared.

Trimmed flight conditions resulting from the combinations of Mach number and altitude are used. It is observed that, for the IC3X, the definition of the temperature field presents the largest effect on maximum absolute strain values on the inner surface of the vehicle. In fact, thermal effects can account for 97.7–99.5% of total maximum absolute strain values. For untrimmed flight conditions, thermal effects can account for 66–100% of total maximum absolute strain values. The cases where thermal effects have the lowest impact on overall strain values are those where dynamic pressure and angle of attack are the highest.

The considered temperature fields present minimum and maximum temperatures on the inner surface of the vehicle that range between 41–414 K and 398–914 K, respectively.

Even though there seems to be an overestimation of the strain values due to thermal effects, these results highlight the importance and necessity of appropriately considering the thermal effects for this vehicle-as-a-sensor concept in high-speed flight.

The strain estimation can be improved by considering more realistic thermal loads. In the current implementation in Abaqus for the thermoelastic problem, the default reference is 0 K. This creates additional thermal strain to the system that are not actually present there. A more realistic reference condition would be room temperature or whatever is the closest to the zero strain under no loads (impacted by manufacturing and assembly processes). This is not a limitation of the methodology and any reference temperature can be accommodated as long as it is defined upfront.

4.2 Sensor Selection

As the problem of sensor selection is separated in two parts, the nodes on the inner surface of the vehicle are ranked twice. One ranking considers the importance of strain values on the recovery of aerodynamic loads, and the other considers the importance of temperature values on the recovery of modal coordinates, that were used to generate the temperature fields by combining the thermal POD modes.

4.2.1 Strain

As mentioned in Subsection 3.1, the distributed loads applied on the vehicle are modeled through POD modes. So, for the results presented next, force in the z direction (opposed to gravity but in body frame) is used, and 12 modes are retained on the truncated bases. This results in a half mean squared error of the order of 10^{-30} when comparing the original and the recovered forces.

Using the training data without any thermal effects, the $[C]$ matrix is obtained using Equation 1. The modal coordinates are recovered with Equation 2, and this results in a half mean squared error of the order of 10^{-12} when comparing to the original forces.

For the ranking of the sensors through the pseudo-inverse of $[C]$, only absolute values of the matrix are considered and each mode is given the same weight. The ranking specifies the node and the strain component of most influence on the recovery of the modal coordinates of the applied forces.

The half mean squared error on the recovery of the nodal forces according to the number of retained sensors after ranked can be seen in Figure 3. There are 14,034 nodes available on the inner surface of the vehicle as sensor points, and considering 6 strain components for each node results in a total of 84,204 possible sensors.
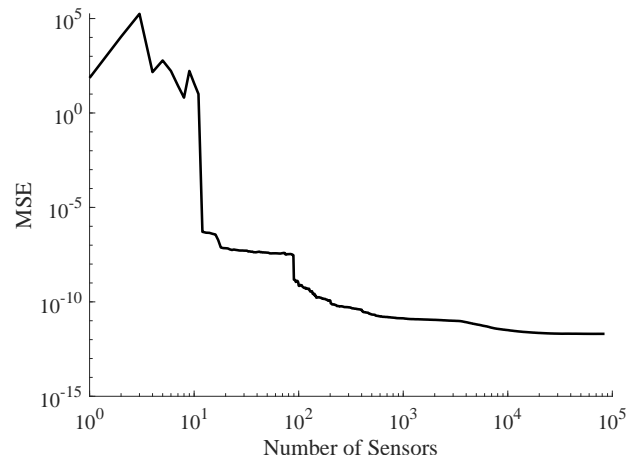

Figure 3: Half mean squared error on recovery of applied forces according to retained number of sensors.

Notice that with 12 retained sensors there is a considerable drop in the error value to 5.1×10^{-7}, with 90 retained sensors the error further decreases to 1.5×10^{-9}, and then with 2,405 retained sensors the error reaches 1×10^{-11}. The locations for these retained sensors can be seen in Figure 4, where the nodes on the inner surface of the IC3X are represented in green and the strain sensor locations are highlighted in black.

For 12 sensors, all of the locations are near the back of the vehicle at a region that presents high stress concentration due to sharp corners. For 90 sensors some locations appear near the nose of the vehicle, and for 2,405 sensors a bulk of the points appear along the vehicle.

This method results in clustered locations due to the high discretization of the possible sensing points and no consideration for optimizing the number of sensors. Notably, for the vehicle-as-a-sensor concept, clustering of sensors might be beneficial, since the use of continuous fiber optic

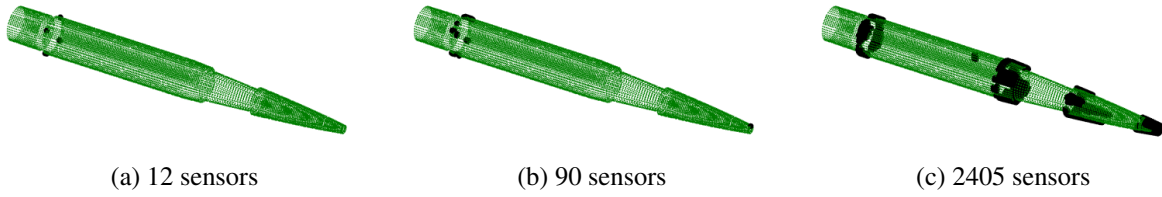(a) 12 sensors   (b) 90 sensors   (c) 2405 sensors

Figure 4: Nodes on the inner surface of the IC3X, with strain sensor points highlighted in black.

strain sensing cables naturally enables it.

However, a selection of 16 sensors based on "engineering judgement" results in an error of 3.4×10^{-9} compared to 3.7×10^{-7} obtained from this method. These sensors were selected by keeping the initial set of 12 and adding the subsequent four that presented the largest contribution to error reduction, and where the distribution of sensor points looks similar to the set represented in Figure 4 (b). The error results are summarized in Table 1.

Table 1: Half mean squared error (MSE) on applied forces.

			Recovered with specified number of sensors				
			Ranked based on heat map				*Selected*
	POD	**All**	**12**	**90**	**2,405**	**16**	**16**
MSE	10^{-30}	10^{-12}	5.1×10^{-7}	1.5×10^{-9}	1×10^{-11}	3.7×10^{-7}	3.4×10^{-9}

4.2.2 Temperature

Similarly to the strain sensor selection, the pseudo-inverse of the thermal modes matrix $[\phi]$ is used for the ranking of the sensor points considering only absolute values and sensor locations on the inner surface of the IC3X. In this case, the ranking specifies only the location of the node of most influence on the recovery of the modal coordinates used to generate the representative temperature fields.

The half mean squared error on the recovery of the thermal modal coordinates according to the number of retained sensors after ranked can be seen in Figure 5. Here, the total number of sensors corresponds to the total number of available nodes, that is, 14,034.

With 35 retained sensors there is a considerable drop in the error value; however, the error is still high. With 79 retained sensors the error is 6.5×10^{-8}, and with 166 retained sensors the error further decreases to 5.8×10^{-10}. The locations for these retained sensors can be seen in Figure 6, where again the nodes on the inner surface of the IC3X are represented in green and the temperature sensor locations are highlighted in black.

According to the sensitivity observed in the thermal modes matrix, the first set of sensors that ranked the highest are located as close as possible to the nose of the vehicle. This region is closest to the Tungsten nose ballast, as defined by Klock and Cesnik [21], which is one of the areas that heats up the most due to the high thermal loads. Interestingly, the method also resulted in a selection of nodes that spanned the whole circumference of that section, which allows for recovering information that is not axisymmetric.

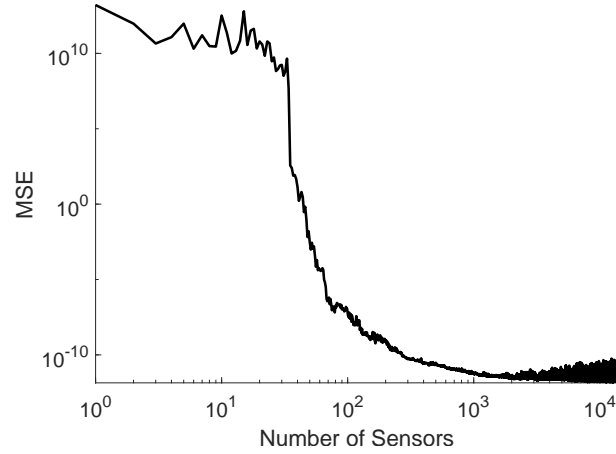When the set with 79 sensors is considered, some information at the back of the vehicle is

Figure 5: Half mean squared error on recovery of applied thermal modal coordinates according to retained number of sensors.

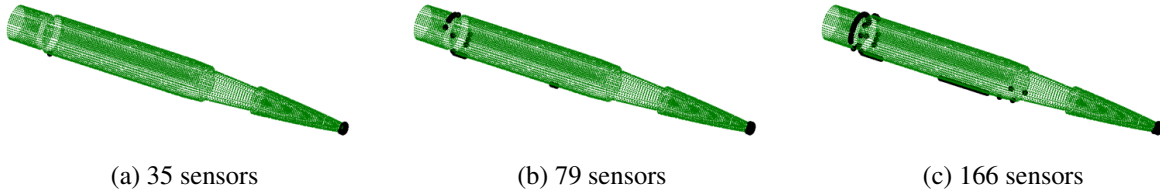| (a) 35 sensors | (b) 79 sensors | (c) 166 sensors |

Figure 6: Nodes on the inner surface of the IC3X, with temperature sensor points highlighted in black.

added, and the remaining selected sensors are located on the lower part of the vehicle in a line, providing for lengthwise spatial discretization.

Similarly to what was observed for the strain sensor selection, if engineering judgement is used to select a set of 42 sensors the error reduces to 5.4×10^{-3} compared to 3.1 obtained through this heat-map method. This set consisted of the 35 sensors represented in Figure 6 (a) and 7 extra sensors located at the back of the vehicle. The error results are summarized in Table 2.

Table 2: Half mean squared error (MSE) on recovery of applied thermal modal coordinates.

	Ranked based on heat map			*Selected*
	79	**166**	**42**	**42**
MSE	6.5×10^{-8}	5.8×10^{-10}	3.1	5.4×10^{-3}

This shows once more that while this method is useful to obtain the locations with the highest sensitivity to the loads, it does not consider any optimization on the number of sensors retained. However, it does provide insight into the desirable sensor locations that can be used to infer the sensor selection.

4.3 Recovery of Pressure Distribution

As addressed in Subsection 2.3, the inverse model predicts the pressure distribution through the recovery of modal coordinates. The pressure bases were truncated in a similar manner as Weston and Cesnik [17] applied on the thermal model. The first pressure mode was omitted from the metric, and 99.99% of the cumulative sum of the remaining eigenvalues was obtained

when a total of 7 modes are retained. When considering the non-dimensionalized pressure values on the outer surface elements of the vehicle and the flight conditions of interest, the half mean squared error of the truncated model is 2.5×10^{-4}.

As an example, the pressure distribution on the outer surface of the IC3X can be seen in Figure 7, where pressure values obtained through Newtonian impact theory with shock-expansion relations are compared with pressure values recovered with the 7 retained POD modes. The largest difference is observed near the nose region, and it is smaller than 3%.
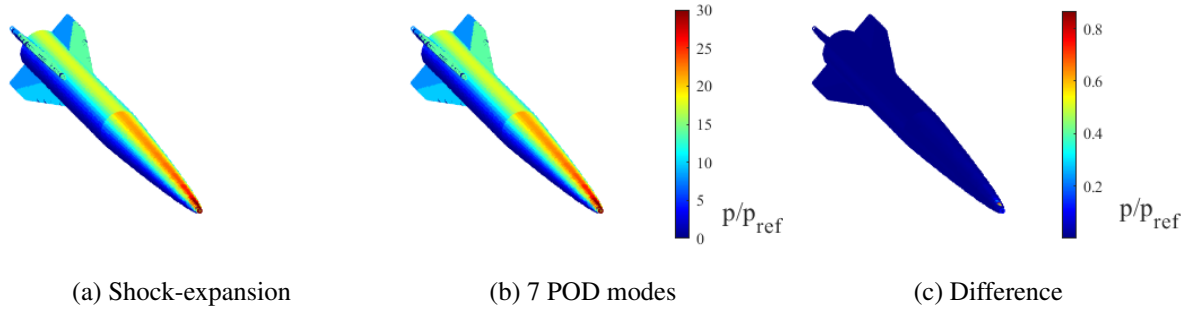

   (a) Shock-expansion   (b) 7 POD modes   (c) Difference

Figure 7: Comparison of pressure distribution on the outer surface of the IC3X at Mach 6, 20-km altitude and angle of attack of 30°.

Considering the untrimmed training data generated with no thermal effects, the pressure recovered through a neural network-based inverse model with 54 strain sensors, as ranked in Subsection 4.2.1 and referred here as **Set 1**, can be seen in Figure 8. Differences in pressure values when compared to shock-expansion, as well as to pressure recovered with 7 POD modes, are largest in the nose, accounting for 3.7% and 3.4%, respectively.
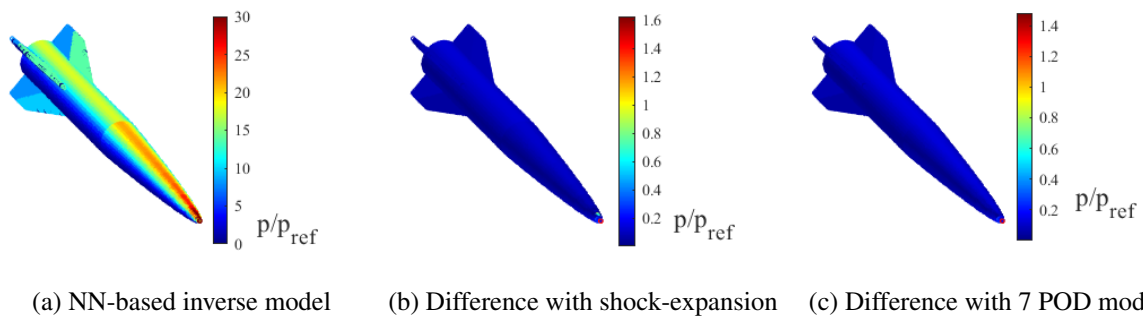

(a) NN-based inverse model   (b) Difference with shock-expansion   (c) Difference with 7 POD modes

Figure 8: Comparison of recovered pressure distribution on the outer surface of the IC3X at Mach 6, 20-km altitude and angle of attack of 30°, through a NN-based inverse model.

The half mean squared error observed for all 60 flight conditions available and on all the panels on the outer surface of the vehicle when compared to shock-expansion is 5×10^{-2}. While considerably larger than what was obtained for truncating the model with POD, it shows that recovery of pressure through a NN-based inverse model with a reduced set of sensors is feasible.

The actual accuracy is highly dependent on the outcome of the optimization process used to obtain the neural network model, and the number of training data cases available. It is considered good practice not to have more sensors than the number of training data cases. Comparisons for inverse models trained with different sets and number of sensors are not carried out, since

11

defining a well optimized comparable solution for each trained NN can be tricky. For the results shown here, the coefficient of determination (R^2) for recovery of each of the 7 modal coordinates was larger than 0.9, and can be found in Table 3. Setting up the problem with different numbers of sensors results in NNs with diverse characteristics (weights, biases, number of layers, number of nodes per layer, activation functions), such that the difference in accuracy observed cannot be said to be due to the selection of sensors. The main parameters of the neural networks considering the recovery of each of the modal coordinates c and each of the conditions to be discussed next, with and without the inclusion of thermal effects, are summarized in Table 3.

Table 3: Parameters of the neural networks, where c_i corresponds to the i-th modal coordinate used to recover the pressure distribution, n_{lay} corresponds to the number of layers, n_{nodes} corresponds to the number of nodes in each layer, **Act.** indicates the type of activation function, **Stand.** indicates if standardization was applied, λ corresponds to the regularization term strength, and R^2 corresponds to the coefficient of determination.

Thermal?	Set	c_i	n_{lay}	n_{nodes}	Act.	Stand.	λ	R^2
No	1	1	2	[97,385]	Sigmoid	Yes	0.1081	0.9995
		2	2	[53,381]	Sigmoid	Yes	0.1003	0.9907
		3	1	[55]	Sigmoid	Yes	0.0046	0.9986
		4	3	[2,1,205]	tanh	Yes	3.53×10^{-6}	0.956
		5	1	[322]	tanh	Yes	0.0254	0.9553
		6	1	[3]	Sigmoid	Yes	2.43×10^{-5}	0.9171
		7	5	[17,8,5,2,275]	tanh	Yes	0.0369	0.9828
Yes	1	1	4	[122,112,118,81]	ReLU	Yes	2.0884	0.9647
		2	2	[222,287]	ReLU	Yes	1.7812	0.9191
		3	3	[177,56,213]	tanh	Yes	0.9643	0.8653
		4	4	[131,2,68,339]	none	Yes	0.1666	0.338
		5	1	[1]	ReLU	Yes	6.18×10^{-4}	0.2854
		6	5	[172,4,97,6,134]	ReLU	Yes	0.0015	0.5651
		7	3	[3,7,73]	tanh	Yes	0.0029	0.4013
Yes	2	1	5	[84,128,260,159,144]	ReLU	Yes	0.1583	0.9669
		2	3	[355,204,231]	tanh	Yes	4.6778	0.9384
		3	3	[307,388,347]	tanh	Yes	0.1346	0.9146
		4	3	[27,379,145]	tanh	Yes	7.94×10^{-9}	0.5036
		5	5	[75,8,375,229,135]	tanh	Yes	0.0024	0.6155
		6	4	[60,1,2,88]	tanh	Yes	1.30×10^{-7}	0.4551
		7	5	[17,2,7,13,2]	ReLU	No	7.58×10^{-9}	~ 0
Yes	3	1	4	[88,290,288,170]	ReLU	Yes	0.1228	0.9648
		2	3	[261,30,235]	tanh	Yes	8.6887	0.9436
		3	3	[396,269,325]	tanh	Yes	0.0916	0.934
		4	5	[295,3,176,14,277]	none	Yes	5.72×10^{-9}	0.3088
		5	4	[38,224,398,89]	tanh	Yes	4.89×10^{-7}	0.6081
		6	4	[274,62,355,17]	tanh	Yes	1.95×10^{-8}	0.5601
		7	5	[22,24,5,379,1]	ReLU	No	3.39×10^{-6}	~ 0

For an adequate recovery of modal coordinates for the error evaluation on the temperature sensor selection in Subsection 4.2.2, at least 32 temperature fields are needed. Thus, for conservative purposes 34 representative temperature fields were generated for obtaining the training data with thermal effects.

Considering the same 54 selected sensors (**Set 1**) and strain measurements only on the train-

ing data set with thermal effects, the pressure distribution difference with the reference shock-expansion for a case at temperature of 0 K can be seen in Figure 9 (a). The error observed increased to 13.2%, however, the trained neural network only presented a coefficient of determination larger than 0.9 for 2 out of the 7 modal coordinates. The half mean squared error observed for all 60 flight conditions available and on all the panels on the outer surface of the vehicle when compared to shock-expansion is 1.06. This indicates that the neural network was not able to properly fit the available data, which is expected since thermal effects have a large impact on the strain values and no temperature measurements were considered. Pressure distribution difference on a temperature state different than 0 K (temperature field 1) can be seen in Figure 10 (a). The maximum error observed was 6.7%. This temperature field ranges between 178–620 K on the vehicle's inner surface.
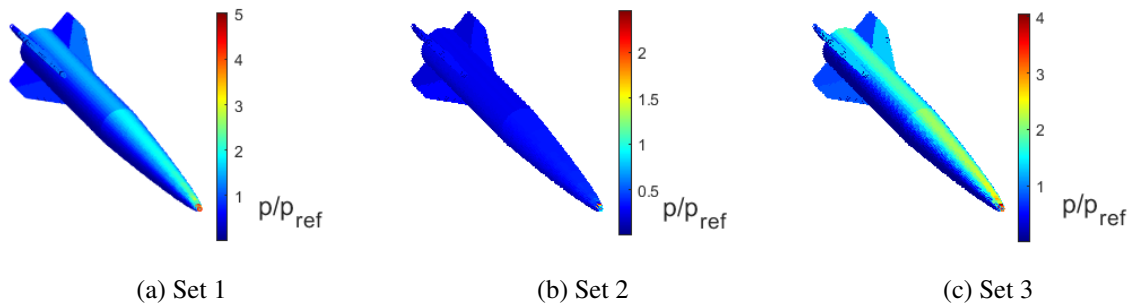
(a) Set 1	(b) Set 2	(c) Set 3

Figure 9: Difference of recovered pressure distribution with shock-expansion on the outer surface of the IC3X at Mach 6, 20-km altitude and angle of attack of 30°, and temperature of 0 K.
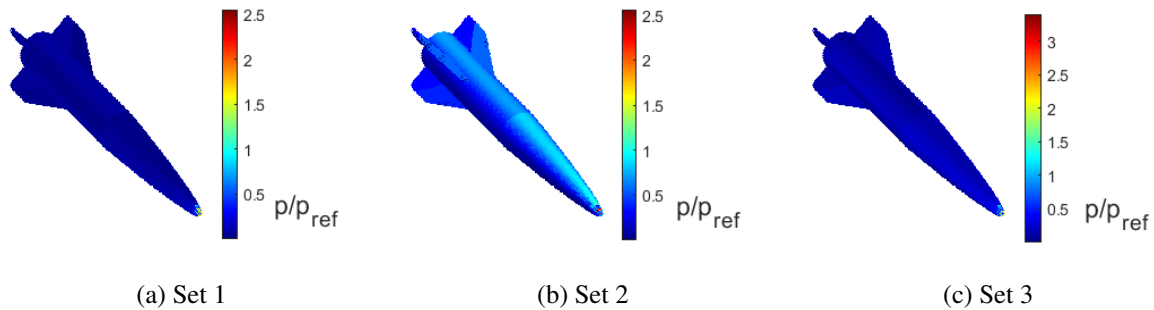
(a) Set 1	(b) Set 2	(c) Set 3

Figure 10: Difference of recovered pressure distribution with shock-expansion on the outer surface of the IC3X at Mach 6, 20-km altitude and angle of attack of 30°, and temperature field 1.

When adding temperature measurements to the same 54 selected sensor locations, referred here as **Set 2**, the pressure distribution difference with the reference shock-expansion for a representative case can be seen in Figure 9 (b). The maximum error observed decreased to 6.4%, and the trained neural network presented a coefficient of determination larger than 0.9 for 3 out of the 7 modal coordinates. The half mean squared error observed for all 60 flight conditions available and on all the panels on the outer surface of the vehicle when compared to shock-expansion decreased to 0.94. This indicates that the neural network still was not able to properly fit the available data, however there was an improvement when compared to not having any temperature measurements. Pressure distribution for temperature field 1 can be seen in Figure 10 (b). The maximum error observed was 6.7%.

Consider now the 54 strain sensors selected through the ranking of the strain sensors and 54

13

temperature sensors selected through the ranking of the temperature sensors, referred here as **Set 3**. For this set, the pressure distribution difference with the reference shock-expansion for a representative case can be seen in Figure 9 (c). The maximum error observed is 10.6%, and the trained neural network presented a coefficient of determination larger than 0.9 for 3 out of the 7 modal coordinates. The half mean squared error observed for all 60 flight conditions available and on all the panels on the outer surface of the vehicle when compared to shock-expansion decreased to 0.96. This also indicates that the neural network still was not able to properly fit the available data, and that using the temperature sensors selected through the temperature sensor selection metric did not necessarily provided for better results than using the temperature sensors selected through the strain sensor selection approach. Pressure distribution for temperature field 1 can be seen in Figure 10 (c). The maximum error observed was 8.9%. Table 4 summarizes the errors for the purely aeroelastic problem and the aerothermoelastic one.

Table 4: Half mean squared error (MSE) on recovery of non-dimensional pressure for problems where the thermal effects are and are not present.

		Thermal effects present?			
		No	*Yes*		
	POD	**Set 1**	**Set 1**	**Set 2**	**Set 3**
MSE	2.5×10^{-4}	5×10^{-2}	1.06	0.94	0.96

The difficulties observed in obtaining a good fit for the inverse model in the presence of thermal effects could be improved by increasing the number of samples in the training data. Increasing the number of temperature states as well as the discretization of flight conditions would also allow for increasing the number of sensors considered in the inverse model. This shows the necessity of having training data of adequate quality (in terms of sensor selection) and quantity for the application of neural networks to this problem.

The strain values considering thermal effects are likely being overestimated due to high temperature values currently applied, and this could also be inducing an extra level of difficulty that is unrealistic.

Even with all this considered, a neural network inverse model that uses as inputs strain and temperature measurements on the internal structure of a vehicle is still a promising approach for the recovery of pressure distribution on the vehicle's outer surface in flight. Further investigations are ongoing and will be reported at a later time.

5 CONCLUDING REMARKS

A neural network-based inverse model is applied to a vehicle-as-a-sensor concept in high-speed flight. This concept aims to address current difficulties regarding sensors on the outer surface of a vehicle used to obtain its aerodynamic state, particularly in hypersonic flight conditions.

The framework for generating the data used to train the neural network is formulated, where representative aerodynamic loads and temperature fields spanning the parameter space observed in flight are applied to a detailed finite element model of the vehicle. The process to include thermal effects is described, where temperature fields obtained through combinations of a POD basis resulting from possible temperatures observed in flight are generated and applied to a thermoelastic solution of the equilibrium equations.

A feedforward fully connected neural network for regression is trained to predict pressure distri-

bution given strain and temperature measurements. Recovery of modal coefficients of a reduced order model of the pressure distribution is applied to make the problem more tractable.

A sensor selection methodology consisting of obtaining the sensitivity of a sensing point to the applied loads is evaluated. The problem was separated in two parts, where a strain sensor ranking was obtained for recovery of force and a temperature sensor ranking was obtained for recovery of the thermal modal coordinates used to generate the representative temperature distribution in the vehicle. While the error on recovery of loads according to the number of sensors was quantified, the results showed clustering of sensor locations, and an optimization on the number of sensors for a given error threshold was not considered.

Inverse models considering the selected sensors were trained and the error on recovery of pressure distribution was compared. While the recovery of pressure is feasible, and the inclusion of temperature sensors shows an increase in accuracy of this recovery, difficulties were observed in obtaining a well-trained neural network given the current sensor set and NN parameter choices.

Future work includes improving the sensor selection process by considering optimal sensor placement techniques, and improving the neural network's capability to recover pressure by using more accurate and adequate sampling of the training data.

6 ACKNOWLEDGMENTS

7 REFERENCES

[1] Bowcutt, K., Finley, D., Hagseth, P., et al. (2023). Lecture Notes in Hypersonic Flight Vehicle Design and Performance Analysis - Online Short Course. AIAA.

[2] Pham, J., Morreale, B. J., Clemens, N., et al. (2022). Aerodynamic Sensing for Hypersonics via Scientific Machine Learning. In *AIAA AVIATION Forum*. doi:https://doi.org/10.2514/6.2022-3717.

[3] Falkiewicz, N. J. and Cesnik, C. E. S. (2017). Enhanced Modal Solutions for Structural Dynamics in Aerothermoelastic Analysis. *Journal of Aircraft*, 54(3), 870–889. doi:https://doi.org/10.2514/1.C034122.

[4] Anderson Jr., J. D. (2006). *Hypersonic and High-Temperature Gas Dynamics*. AIAA, 2nd ed. ISBN 978-1-56347-780-5.

[5] Maniatty, A., Zabaras, N., and Stelson, K. (1989). Finite Element Analysis of Some Inverse Elasticity Problems. *Journal of Engineering Mechanics*, 115(6), 1303–1317. doi:https://doi.org/10.1061/(ASCE)0733-9399(1989)115:6(1303).

[6] Shkarayev, S., Krashanitsa, R., and Tessler, A. (2001). An Inverse Interpolation Method Utilizing In-Flight Strain Measurements for Determining Loads and Structural Response of Aerospace Vehicles. Tech. rep., NASA Langley Technical Report Server.

[7] Martin, T. J., Halderman, J. D., and Dulikravich, G. S. (1995). An Inverse Method for Finding Unknown Surface Tractions and Deformations in Elastostatics. *Computers & Structures*, 56(5), 825–835. ISSN 0045-7949. doi:https://doi.org/10.1016/0045-7949(95)00011-5.

[8] Pham, J., Ghattas, O., and Willcox, K. E. (2024). Real-Time Aerodynamic Load Estimation for Hypersonics via Strain-Based Inverse Maps. In *AIAA SCITECH 2024 Forum*. doi:https://doi.org/10.2514/6.2024-1228.

[9] Panigrahi, A., Nguyen, A. Q., Eitner, M. A., et al. (2024). Strain-Data Driven Force Reconstruction Using Pseudo-Inverse Matrix. In *IMAC-XLII 2024 Conference*.

[10] Raissi, M., Perdikaris, P., and Karniadakis, G. E. (2019). Physics-Informed Neural Networks: A Deep Learning Framework for Solving Forward and Inverse Problems Involving Nonlinear Partial Differential Equations. *Journal of Computational Physics*, 378, 686–707. ISSN 0021-9991. doi:https://doi.org/10.1016/j.jcp.2018.10.045.

[11] Singh, V. and Willcox, K. E. (2017). Methodology for Path Planning with Dynamic Data-Driven Flight Capability Estimation. *AIAA Journal*, 55(8), 2727–2738. doi:https://doi.org/10.2514/1.J055551.

[12] Cao, X., Sugiyama, Y., and Mitsui, Y. (1998). Application of Artificial Neural Networks to Load Identification. *Computers & Structures*, 69(1), 63–78. ISSN 0045-7949. doi:https://doi.org/10.1016/S0045-7949(98)00085-6.

[13] Klotz, T., Pothier, R., Walch, D., et al. (2021). Prediction of the Business Jet Global 7500 Wing Deformed Shape Using Fiber Bragg Gratings and Neural Network. *Results in Engineering*, 9, 100190. ISSN 2590-1230. doi:https://doi.org/10.1016/j.rineng.2020.100190.

[14] Klock, R. and Cesnik, C. E. S. (2014). Aerothermoelastic Simulation of Air-Breathing Hypersonic Vehicles. In *55th AIAA/ASME/ASCE/AHS/ASC Structures, Structural Dynamics, and Materials Conference*. doi:https://doi.org/10.2514/6.2014-0149.

[15] Gentry, A. E. and Smyth, D. N. (1968). Hypersonic Arbitrary-Body Aerodynamic Computer Program, Mark III Version, Volume II, Program Formulation and Listings. Tech. rep., Douglas Report DAC 61552.

[16] Meinicke, A. C. and Cesnik, C. E. S. (2024). On the Efficient Generation of Training Data for High-Speed Aerodynamic State Recovery Through Strain-Load Neural Network Model. In *AIAA SCITECH 2024 Forum*. doi:https://doi.org/10.2514/6.2024-1047.

[17] Weston, C. S. and Cesnik, C. E. S. (2024). Hybrid-Fidelity Global-Local Aerothermoelastic Modeling for Hypersonic Flight. In *AIAA SCITECH 2024 Forum*. doi:https://doi.org/10.2514/6.2024-1045.

[18] Smith, M. (2009). *ABAQUS/Standard User's Manual, Version 6.9*. United States: Dassault Systèmes Simulia Corp.

[19] Lundberg, S. M. and Lee, S.-I. (2017). A Unified Approach to Interpreting Model Predictions. In *31st International Conference on Neural Information Processing Systems*. pp. 4768–4777. doi:https://doi.org/10.48550/arXiv.1705.07874.

[20] Klock, R. J. and Cesnik, C. E. S. (2017). Nonlinear Thermal Reduced-Order Modeling for Hypersonic Vehicles. *AIAA Journal*, 55(7), 2358–2368. doi:https://doi.org/10.2514/1.J055499.

[21] Klock, R. and Cesnik, C. E. S. (2015). Aerothermoelastic Reduced-Order Model of a Hypersonic Vehicle. In *AIAA Atmospheric Flight Mechanics Conference*. doi:https://doi. org/10.2514/6.2015-2711.

COPYRIGHT STATEMENT